J. Fluid Mech. (2022), *vol*. 940, A22, doi:10.1017/jfm.2022.235

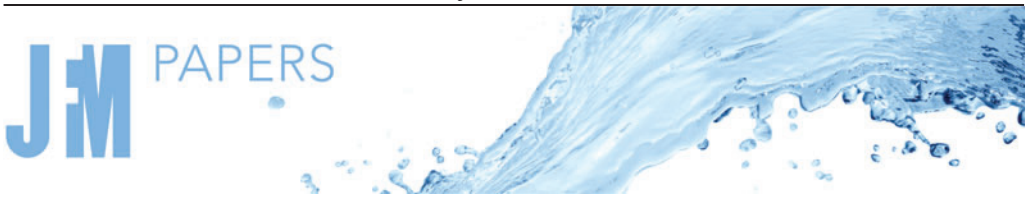

Topological bifurcations in the transition from two single vortices to a pair and a single vortex in the periodic wake behind an oscillating cylinder

Anne R. Nielsen[1], **Puneet S. Matharu**[2] **and Morten Brøns**[1,†]

[1]Department of Applied Mathematics and Computer Science, Technical University of Denmark, 2800 Lyngby, Denmark

[2]School of Mathematics, University of Manchester, Oxford Road, Manchester M13 9PL, UK

(Received 29 August 2021; revised 27 January 2022; accepted 11 March 2022)

We explore the two-dimensional flow past a cylinder undergoing forced transversal oscillations with the aim of elucidating the evolution of the topology of the wake under variation of the forcing amplitude at a Reynolds number of 100. In particular, we study the change from two single vortices (2S mode) to a pair and a single vortex (P + S mode) being shed per period. Matharu *et al.* (*J. Fluid Mech.*, vol. 918, 2021, p. A21) showed that a dynamical symmetry-breaking pitchfork bifurcation plays a key role in this transition. We show that in addition to this bifurcation, a number of topological bifurcations in the vorticity field occur, both on the symmetric 2S branch and on the asymmetric P + S branch. The topological bifurcations are cusp bifurcations where an extremum of vorticity is created or destroyed. To describe the effect of the topological bifurcations we introduce an extended symbolic classification of the wake modes to account for the spatial variations of the vortex patterns that occur in the transition process. We identify four amplitude values that define critical stages in the transition, and provide a complete qualitative picture of the transition from 2S to P + S mode. We confirm the robustness of the observed transition process by simulations at Reynolds number 80.

Key words: bifurcation, vortex streets, topological fluid dynamics

1. Introduction

In this paper, we draw attention to the classical fluid mechanical problem of the flow past a circular cylinder undergoing forced transverse oscillations. The problem is considered a basic case for bluff bodies with more complex geometries, and it contributes to the understanding of vortex-induced vibrations. Periodic wakes behind oscillating bodies have a structure that depends on the body shape as well as external parameters. For example,

† Email address for correspondence: mobr@dtu.dk

Schnipper, Andersen & Bohr (2009) demonstrated that for certain amplitudes and periods of a flapping wing, very complex wake patterns with up to 16 vortices per oscillation cycle can be observed. Further, in a landmark and much-cited paper, Williamson & Roshko (1988) experimentally studied the flow past an oscillating cylinder. Their paper was the first to provide a comprehensive study of the different wake patterns that arise through a variation in the wavelength λ and the amplitude A of the cylinder oscillations. They introduced a classification of the wakes based on the number of vortices that were shed with each cylinder oscillation. With this terminology, S denotes a single vortex, P denotes a pair of vortices of opposite signs, so a pattern such as P + S is one where a pair of vortices and a single vortex are shed in each oscillation cycle. The classification can be used for any periodic vortex wake, even if it is generated by a self-oscillation and not by a periodic forcing. For instance, the well-known periodic Kármán vortex street behind a stationary cylinder is referred to as a 2S wake. Williamson & Roshko (1988) identified several vortex shedding patterns more complex than the 2S wake. In later studies, these complicated wake patterns have become known as 'exotic wakes' (Aref, Stremler & Ponta 2006; Ponta & Aref 2006). There are good reasons why the understanding of wake patterns of a circular cylinder is important. The experiments by Williamson & Roshko (1988) suggested that the variation of the force acting on the cylinder under variation of the forcing frequency found by Bishop, Hassan & Saunders (1964) could be explained by changes in the wake mode. This connection has subsequently been confirmed both for forced oscillations of the cylinder we consider in the present paper (Blackburn & Henderson 1999; Carberry, Sheridan & Rockwell 2001; Morse & Williamson 2009) and for vortex-induced oscillations (Brika & Laneville 1993). For wakes of flapping foils, the topological transition from a von Kármán vortex street to a reverse von Kármán vortex street and its subsequent loss of stability is associated with a change of drag into thrust (Godoy-Diana, Aider & Wesfreid 2008; Dynnikova *et al.* 2021). Furthermore, the wake structure is decisive for transport of passive particles, which has mostly been studied in the context of fixed cylinders. For example, Shariff, Pulliam & Ottino (1991) discuss the connection between streaklines and the vorticity field, and Sandulescu *et al.* (2006) analyse the flow of particles across a wake.

Any qualitative changes of structures in dynamical systems occur through bifurcations. In this paper, we examine the bifurcation phenomena in play when the wake pattern changes from a 2S to a P + S wake under a variation in the oscillation amplitude. Bifurcations can occur at two different levels in fluid dynamical problems: at a dynamical level or at a topological level. At a dynamical level, we consider the Navier–Stokes equations as a dynamical system and the bifurcations of these equations occur in an infinite-dimensional function space of velocity fields. A fixed point of this system corresponds to a steady flow, and a limit cycle to a periodic flow. A classical example of a dynamical bifurcation is the supercritical Hopf bifurcation that occurs when the steady flow past a stationary cylinder loses its stability to a time-periodic solution at $Re \approx 46$ (see, e.g., Dusek, Le Gal & Fraunie 1994; Noack & Eckelmann 1994). The Hopf bifurcation is an absolute instability, where the entire flow oscillates. A convective instability (Huerre & Monkewitz 1990), where a localised disturbance is carried by the flow without decaying, is also a bifurcation phenomenon on the dynamical level. At a topological level, we consider a family of flow fields that are already available from solving Navier–Stokes equations at different parameter values. Bifurcations at a topological level are not associated with any loss of stability, but result in changes to the topology of a flow field such as velocity or vorticity. An example of a topological bifurcation is the creation of the two symmetric recirculation zones in the steady flow past a stationary cylinder when $Re \approx 5$ (see, e.g.,

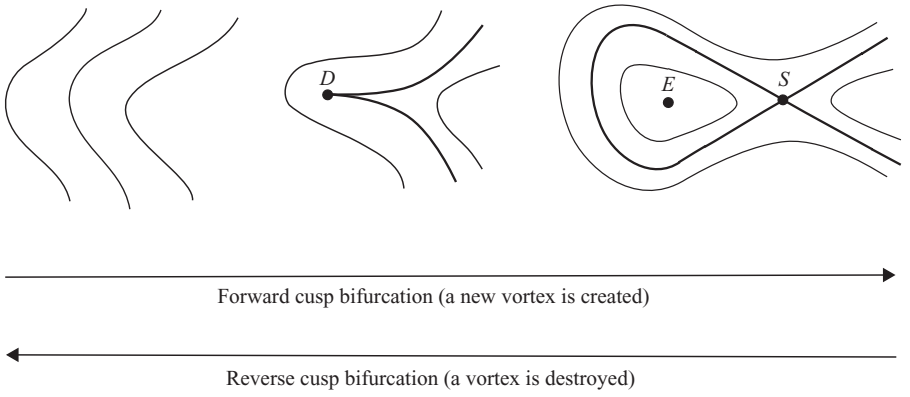

Figure 1. The vorticity topology during a cusp bifurcation when a parameter is varied. Going from left to right, the level curves of vorticity deform to create an ordinary cusp singularity at the degenerate critical point D. With a further change of the parameter a saddle S and an extremum E emerge which results in the formation of a vortex. The process going right to left is the destruction of a vortex.

Brøns *et al.* 2007). Bifurcations can occur at both levels, but in general they are not related. Heil *et al.* (2017) show that the formation of the Kármán-vortex street is a result of both types of bifurcations occurring at two distinct, but very close values of the Reynolds number; the transition from a steady to a time-periodic flow is a dynamical bifurcation, and the transition of the shear layer into individual vortices is a topological bifurcation of the vorticity field that occurs at a slightly higher Reynolds number.

In order to describe the topological changes that occur in the wake, we require a clear definition of the topological structures to be considered. Here, we analyse the topology of the flow field in terms of the vorticity field ω. Since we consider a two-dimensional flow, ω is a scalar field whose topology is described by the level curves and the critical points at which $\partial_x\omega = \partial_y\omega = 0$. The type of a critical point is determined by the determinant of the Hessian matrix

$$|\boldsymbol{H}^{\omega}| = \partial_{xx}\omega\partial_{yy}\omega - (\partial_{xy}\omega)^2. \tag{1.1}$$

If $|\boldsymbol{H}^{\omega}| > 0$ the critical point is an extremum and if $|\boldsymbol{H}^{\omega}| < 0$ it is a saddle point. An extremum in the vorticity field is encircled by closed level curves, and such a region is often identified as a vortex. As long as extrema or saddles are regular (i.e. $|\boldsymbol{H}^{\omega}| \neq 0$), they are robust, and are advected with the flow; see Brøns & Bisgaard (2010) for a derivation of their equations of motion. To locate any topological changes in the vorticity field we must therefore locate the degenerate critical points where $|\boldsymbol{H}^{\omega}| = 0$. Under generic assumptions on higher-order derivatives of ω it can be shown (Brøns 2007) that the simplest possible change in the topology is a cusp bifurcation (also known as a saddle-centre bifurcation). A cusp bifurcation occurs when $\boldsymbol{H}^{\omega}$ has zero as a simple eigenvalue, that is, when $|\boldsymbol{H}^{\omega}| = 0$ and $\mathrm{tr}(\boldsymbol{H}^{\omega}) \neq 0$. The level curves and the critical points of the vorticity field during a cusp bifurcation are illustrated in figure 1. The bifurcation parameter can be any parameter upon which the problem depends. In the present study, we find that several vortices appear or disappear via cusp bifurcations in the flow when time is considered the bifurcation parameter. In order to give an accurate description of the topology of the wake, we introduce an extended symbolic classification which, in contrast to Williamson and Roshko's terminology, accounts for topological variations in the downstream wake. Our extended classification is introduced in § 4.

The 2S wake preserves a spatio-temporal Z_2 symmetry (Blackburn, Marques & Lopez 2005), which means that if the flow is evolved forward in time by half a period, and is reflected spatially about the wake centreline, then the original wake pattern is recovered. In terms of the vorticity field, it implies

$$\omega(x, y, t) = -\omega(x, -y, t + 1/2), \tag{1.2}$$

when the period of the cylinder oscillations is normalised to one. It is clear that a P + S wake pattern cannot satisfy the same condition as it alternates between a single vortex or a pair of vortices being shed in every half period.

In a very recent paper, Matharu, Hazel & Heil (2021) examined the dynamical bifurcations that lead to symmetry breaking. They considered the fundamental lock-in region where the cylinder oscillates with the Strouhal frequency of the cylinder and show that, at $Re = 100$, the loss of symmetry is due to a subcritical pitchfork bifurcation at a dynamical level. In § 5, we analyse the topological role of the symmetry-breaking pitchfork bifurcation. We prove that the dynamical bifurcation relaxes the condition that two cusp bifurcations must occur with an exact temporal spacing of half a period. This allows one of the bifurcation points to move rapidly downstream. By monitoring the structural changes of the vorticity field we show that the pitchfork bifurcation plays an important role in the transition from 2S to P + S mode. However, it is also clear that it does not provide the complete topological description. In this paper, we show that the transition is the result of a sequence of topological bifurcations with some occurring while the wake remains symmetrical. We confirm the robustness of the scenario at $Re = 100$ by simulations at $Re = 80$.

2. Problem setup

We study the two-dimensional flow past a transversely oscillating cylinder in a finite-width channel. The cylinder is prescribed to oscillate with period T and amplitude A for a specified inflow velocity U. Instead of the period, we consider the wavelength $\lambda = UT$ as an equivalent parameter. Figure 2 shows a sketch of the setup. We non-dimensionalise the velocity field $\boldsymbol{u}$ by rescaling with U. All lengths, including the amplitude A and the wavelength λ, are non-dimensionalised on the diameter of the cylinder, D. The pressure p is scaled on the associated viscous scale, $\mu U/D$, where μ is the dynamic viscosity of the fluid, and time is scaled on the advective timescale, D/U. The flow (in the moving frame of reference) is then governed by the non-dimensional Navier–Stokes equations

$$Re\left(\frac{\partial \boldsymbol{u}}{\partial t} + (\boldsymbol{u}\cdot\boldsymbol{\nabla})\boldsymbol{u}\right) = -\boldsymbol{\nabla}p + \nabla^2\boldsymbol{u} \quad \text{and} \quad \boldsymbol{\nabla}\cdot\boldsymbol{u} = 0, \tag{2.1a,b}$$

where the Reynolds number is $Re = \rho UD/\mu$, with ρ being the density of the fluid. In the moving frame of reference we use a Cartesian coordinate system, in which the centre of the cylinder is located at

$$x_{cyl}(t) = 0, \quad y_{cyl}(t) = A\sin(2\pi t/\lambda). \tag{2.2a,b}$$

On the surface of the moving cylinder we impose the no-slip condition

$$u = 0, \quad v = \frac{\mathrm{d}y_{cyl}}{\mathrm{d}t} = (2\pi A/\lambda)\cos(2\pi t/\lambda). \tag{2.3a,b}$$

We also impose the boundary conditions

$$u = 1, \quad v = 0, \quad \text{at } x = -L_{inlet} \text{ and at } y = \pm H/2, \tag{2.4}$$

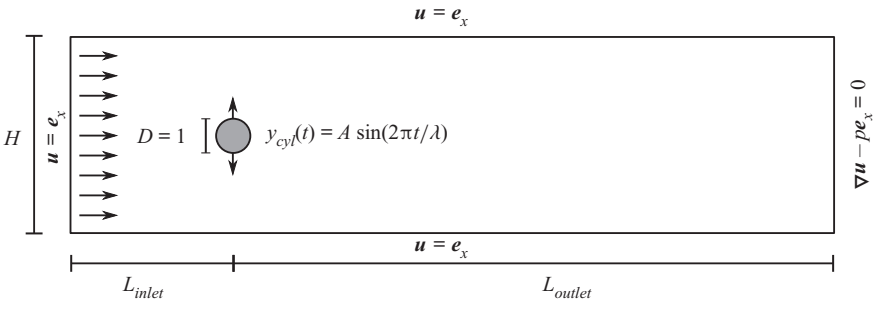

Figure 2. Sketch of the problem setup and the boundary conditions, all expressed in non-dimensional variables. The setup is described by a Cartesian coordinate system where the origin coincides with the centre of the cylinder at $t = 0$.

corresponding to a uniform inflow and a no-slip condition relative to the moving channel walls. Furthermore we allow the outlet to remain (pseudo-)traction free, i.e.

$$\begin{pmatrix} -p + \partial u/\partial x \\ \partial v/\partial x \end{pmatrix} = \begin{pmatrix} 0 \\ 0 \end{pmatrix} \quad \text{at } x = L_{outlet}. \tag{2.5}$$

In the main computational part of this study we fix the Reynolds number to be 100, well within the regime of two-dimensional flow for a stationary cylinder (Barkley & Henderson 1996). Furthermore, oscillations of the cylinder stabilise the two-dimensional flow (Gioria *et al.* 2009), as also found experimentally by Griffin (1971). We have chosen to use a value of $Re = 100$ so that we can directly compare our results with those by Matharu *et al.* (2021) and Leontini *et al.* (2006).

Our aim is to find time-periodic solutions of (2.1*a*,*b*)–(2.5). For a given solution $\boldsymbol{u}(x, y, t; A, \lambda)$ the corresponding vorticity field can be computed as

$$\omega(x, y, t; A, \lambda) = \nabla \times \boldsymbol{u}(x, y, t; A, \lambda). \tag{2.6}$$

To investigate topological bifurcations in the vorticity field, simulations have been performed at four different values of the wavelength: $\lambda = 5.5$, 6.085, 6.5 and 6.7. The value $\lambda_{St} = 6.085$ is obtained from the relationship

$$T/T_{St} = \lambda_{St} St = 1, \tag{2.7}$$

where T is the period of the imposed cylinder oscillations and T_{St} is the period at which vortices are shed in the same flow past a stationary cylinder, i.e. the Strouhal period. The Reynolds number of $Re = 100$ corresponds to the Strouhal number $St = 0.16434$ when using the Reynolds–Strouhal number relationship given by Williamson (1988). The results for $\lambda = \lambda_{St}$ can be compared directly with the studies by Matharu *et al.* (2021). Having selected the values of the two free parameters, Re and λ, we consider time as the bifurcation parameter and monitor the cusp bifurcations in the vorticity field during a complete oscillation and repeat this as the amplitude is varied.

3. Numerical method

We performed numerical simulations using the open-source finite-element library oomph-lib (Heil & Hazel 2006). The Navier–Stokes equations were spatially discretised with quadrilateral Taylor–Hood elements, within which the velocities and the pressure are represented by quadratic and piecewise linear polynomials, respectively. For the

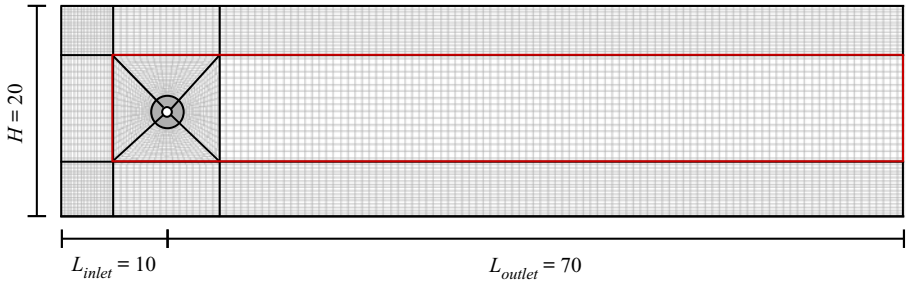

Figure 3. Illustration of the computational domain. The thick black lines show the base mesh and the thin black lines show the mesh after four uniform refinements. In the actual simulations the mesh was uniformly refined five times in the central region (marked with a red box) and three times outside this region.

time-integration of the problem we employ the second-order accurate BDF2 scheme with 320 time steps per period of the imposed oscillations. The simulations were performed on a computational domain with dimensions $H = 20$, $L_{inlet} = 10$ and $L_{outlet} = 70$. The mesh was built from a coarse base mesh and uniformly refined five times. The base mesh is shown with thicker lines in figure 3. In the square central box the nodal positions in the mesh are updated every time step according to the imposed cylinder oscillations. The annular region with unit radius surrounding the cylinder hole is made rigid so that no compression occurs in this part of the mesh as the cylinder oscillates. To reduce the computational cost some of our simulations were performed on a mesh where only the central downstream region and the square central box (highlighted in figure 3 with a red box) were uniformly refined five times whereas the remainder was refined only three times. Upon comparison of mesh types we find no qualitative difference in the vorticity topology.

The simulations are initiated by computing the steady solution for a fixed cylinder at $Re = 0$. We use this result as an initial condition to compute the solution for a slightly higher Reynolds number and continue in this manner until we reach $Re = 100$. This solution is used as an initial condition for the oscillating cylinder simulations where the amplitude of the oscillations is gradually increased in the first two periods. The time-periodicity of the solution is assessed by computing the L^2-norm of the change in the velocity components over one period of the cylinder oscillation. We deem the solution to be time-periodic when the relative change in the L^2-norm of the velocity components drops below 10^{-6}. We have chosen this threshold value by comparing with simulations where the relative change has instead dropped below 10^{-8}. In the cases examined, we observe no topological difference between the two associated vorticity fields, at least not to the level of precision at which we keep track of the cusp bifurcation points.

To compute the vorticity field and its derivatives we first need the derivatives of the velocity field. However, the solution computed via our simulations is only required to be continuous between elements, therefore the derivatives between elements can be discontinuous. To compute smooth approximations of the required derivatives we use the patch-based flux-recovery technique implemented in oomph-lib, which is based on an implementation of the Z2 error estimator (Zienkiewicz & Zhu 1992). For a validation of the method in connection with topological bifurcations see Appendix A of Heil *et al.* (2017). The extrema (and saddle points) are located at the intersections of the nullclines $\partial_x \omega = 0$ and $\partial_y \omega = 0$.

4. An extended classification of wakes with topological variations downstream

When characterising a wake pattern, it is common to use the terminology introduced by Williamson & Roshko (1988). The classification method assumes that the entire wake can be classified as a single type of pattern. Hence, it is implicitly assumed that, once formed, all vortices are translated downstream without any change in the topology. In this section, we argue that a more detailed classification is necessary to be able to describe the wake structure accurately and also to understand the topological changes in the transition from 2S to P + S.

Figure 4 contains snapshots of two different vorticity fields. The vorticity fields have been computed for a cylinder oscillating with the same wavelength but different amplitudes. The feature points for vortices, i.e. the vorticity extrema, are marked with black dots. For $A = 0.80$, we see that two single vortices are shed in each oscillation cycle, and this structure is preserved when the vortices are advected downstream. Therefore, we classify the wake pattern as a full 2S wake. For a larger amplitude of $A = 1.110$ we see a P + S wake pattern that is advected downstream with no topological change. In these examples the terminology introduced by Williamson & Roshko (1988) is fully sufficient for classifying the wake pattern. However, this is not always the case. Figure 5 shows four snapshots of the vorticity field for $A = 1.085$, a value between the cases in figure 4. From the number of vorticity extrema we observe that two pairs of vortices (black dots) are shed during one oscillation cycle, producing a vortex shedding pattern that looks like a 2P mode in the near wake. In each vortex pair one of the vortices is much weaker than the other, and quickly disappears. The black curves in figure 5 encircle a set of vortices shed during an oscillation cycle. In the first snapshot, the encircled region highlights two pairs of vortices. Figure 5(*b*) shows the vorticity field in the last time step before one of the highlighted vortices disappears via a cusp bifurcation with a saddle point. Exactly half a period later, a second cusp bifurcation occurs, and the set of highlighted vortices then consists of two single vortices. The snapshot in figure 5(*b*) shows the last time step before the second cusp bifurcation occurs. Despite the fact that we observe topological bifurcations as the vortices move downstream, the spatio-temporal Z_2 symmetry is preserved throughout the process. Therefore, we conclude that these topological bifurcations are not associated with a loss of symmetry. In order to describe the topological variations of the vorticity field downstream, we introduce an extended classification where we keep track of the pattern of vortices that are created in one cycle, and indicate with a superscript $n \in \mathbb{N}$ how long the pattern persists. If the pattern exists for more than $n - 1$ periods but less than n periods, we designate the superscript n. In the example in figure 5(*b*), the vortices that originate from the same cycle are grouped together with dashed and dotted lines. A dashed line indicates that the group consists of two pairs of vortices, whereas a dotted line indicates that the group consists of two single vortices. We observe that three groups with a 2P pattern are present in the vorticity field just before the first of the two weaker vortices disappears. Hence, we conclude that the vortices in a 2P group move downstream for between two and three periods before any topological bifurcation occur. The wake in figure 5 therefore has a $(2P)^3(2S)^\infty$ vortex pattern. Here ∞ denotes that no further bifurcations are observed in the entire computational domain. In addition, we do not address the changes in the wake structure that occur far downstream. It is well-known that the primary vortex street breaks down into a nearly parallel shear flow with a Gaussian profile at a certain downstream distance, before a secondary vortex street of larger scale may appear further downstream (Karasudani & Funakoshi 1994). Note, that in the extended classification, the standard 2S and P + S wakes are denoted $(2S)^\infty$ and $(P + S)^\infty$, respectively.

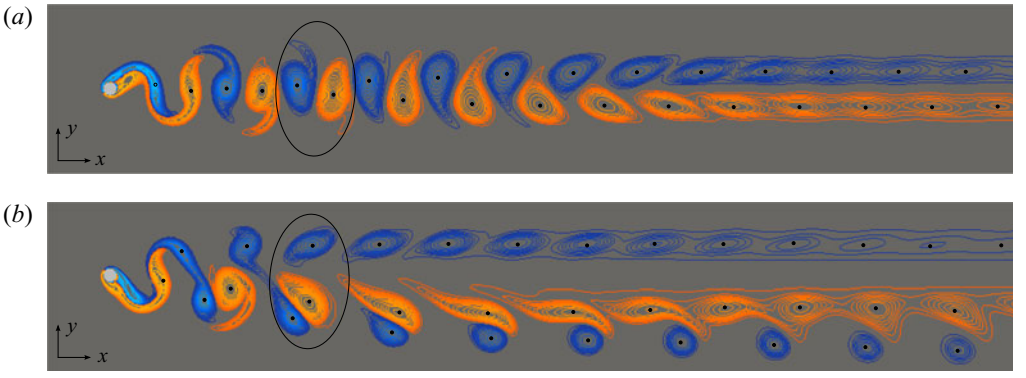

Figure 4. Snapshots of the vorticity field computed at $Re = 100$ for $\lambda = 6.085$ and (*a*) $A = 0.80$ and (*b*) $A = 1.110$. All extrema of vorticity are marked with black dots. The black curves encircle a set of vortices that are shed in a single oscillation cycle. Only part of the computational domain is shown.

Figure 6 shows a snapshot of a vorticity field computed for an oscillating cylinder with $\lambda = 6.7$ and $A = 1.140$. This vorticity field is an example of another wake pattern with topological variations downstream. The snapshot is taken at the last time step before the weaker vortex in the lower pair disappears in a cusp bifurcation. Since this is the only topological bifurcation that occurs, the wake is classified as mode $(2P)^2(P + S)^\infty$. One could argue that the wake patterns in figures 5 and 6 are really just 2S and P + S modes, and the extra vortices that our classification detect in the shear layers have no significant impact. However, as we show in § 5, it is precisely these vortices that become important when describing the topological development from a 2S to a P + S wake.

5. Topological bifurcations of the vorticity field at the symmetry-breaking pitchfork bifurcation point

As mentioned in the introduction, a very recent paper by Matharu *et al.* (2021) showed that the symmetry breaking that occurs in the transition from 2S to P + S mode at $Re = 100$ is due to a dynamical bifurcation, namely a subcritical pitchfork bifurcation. The vorticity field of the 2S wake pattern preserves the spatio-temporal symmetry condition

$$\omega(x, y, t) = -\omega(x, -y, t + 1/2). \tag{5.1}$$

Matharu *et al.* (2021) analysed simulations with increasing amplitude values and construct a bifurcation diagram by measuring the magnitude of the symmetry breaking in the computed solutions. For the vorticity field, the magnitude of the symmetry breaking is given by the norm of the difference between $\omega(x, y, t)$ and $-\omega(x, -y, t + 1/2)$, i.e.

$$\varepsilon = \tfrac{1}{2}\|\omega(x, y, t) + \omega(x, -y, t + 1/2)\|. \tag{5.2}$$

A sketch of their bifurcation diagram is shown in figure 7. At $A = A_2$, a subcritical pitchfork bifurcation occurs, creating two branches of asymmetric time-periodic solutions ω^+, ω^-. Each of these branches subsequently gain stability via fold bifurcations at $A = A_1$. The stable branch associated with $\varepsilon = 0$ corresponds to time-periodic solutions for which the vorticity field satisfies the symmetry condition (5.1), e.g. the 2S wake pattern shown in figure 4(*a*). On the two outer branches of the pitchfork the symmetry condition is broken, meaning that $\varepsilon \neq 0$. The vorticity field of a solution on the positive branch ω^+ has a

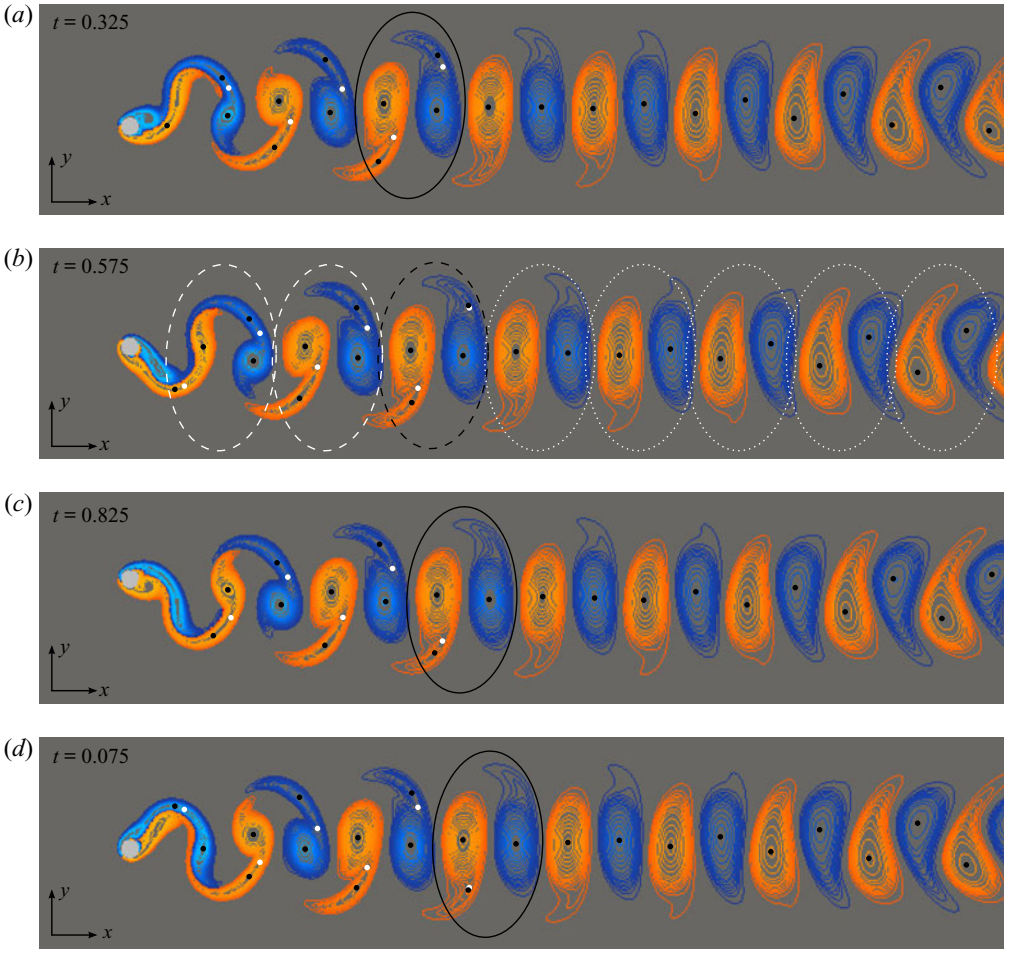

Figure 5. Four snapshots of a vorticity field computed at $Re = 100$ for $\lambda = 6.085$ and $A = 1.085$. The times shown indicate when the snapshots were taken during a single cylinder oscillation with a normalised period of one. All extrema of vorticity are marked with black dots and saddle points are marked with white dots. The black curves highlight how the vortices that are shed in one oscillation cycle move downstream during a period of oscillation. The vortices that originate from the same cycle are grouped together in (*b*). A dashed line indicates that the group consists of two pairs of vortices, whereas a dotted line indicates that the group consists of two single vortices.

conjugate solution on the negative branch ω^- satisfying

$$\omega^+(x, y, t) = -\omega^-(x, -y, t + 1/2). \tag{5.3}$$

We distinguish the bifurcating branches by parameterising ω^+ by ε, and ω^- by $-\varepsilon$. The P + S wake pattern shown in figure 4(*b*) is an example of a wake pattern on the stable part of the ω^- branch, which corresponds to the branch of solutions for which the vortex pair sheds below the centreline. In the conjugate time-periodic solution, which lies on the ω^+ branch, the pair of vortices are instead shed above the centreline. The history of the cylinder motion determines which of the two conjugate solutions a simulation converges to. By reversing the initial motion of the cylinder, we obtain the solution belonging to the opposite branch in the bifurcation diagram. These conjugate solutions correspond to two solutions that satisfy (5.3) on the outer (stable) branches of the pitchfork. As the pitchfork

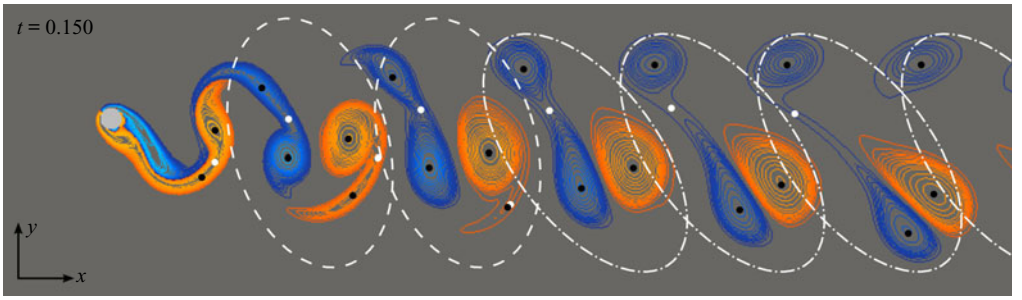

Figure 6. A snapshot of a vorticity field computed at $Re = 100$ for $\lambda = 6.7$ and $A = 1.140$. All extrema of vorticity are marked with black dots and saddle points are marked with white dots. The snapshot is taken at the last time step before a cusp bifurcation occurs. The vortices that originate from the same cycle are grouped together. A dashed line indicates that the group consists of two pairs of vortices, whereas a dash-dotted line indicates that the group consists of a pair and a single vortex.

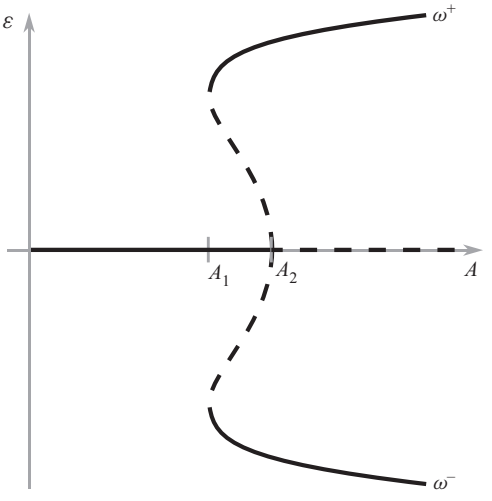

Figure 7. A sketch of the bifurcation diagram illustrating the subcritical pitchfork bifurcation at $A = A_2$ and secondary fold bifurcations at $A = A_1$. In the specific case where the cylinder oscillates with $\lambda = 6.085$, Matharu *et al.* (2021) determined the bifurcation parameter values to be $A_1 \approx 1.0680$ and $A_2 \approx 1.0855$.

is subcritical, three stable periodic solutions exist for amplitudes in the range $A_1 \leq A \leq A_2$, however, the solutions on the branches ω^+ and ω^- are related through the relationship in (5.3) and are identical from a topological point of view; hence we refer to the region as 'bistable' in the following.

In this section, we analyse the topological bifurcations of the vorticity field that occur as a direct result of the dynamical bifurcation. As a starting point for the analysis, we introduce a parameter σ moving along the outer branches in the bifurcation diagram as illustrated in figure 8(*a*). For the sake of simplicity we let $\sigma = 0$ correspond to the symmetric vorticity field located at the pitchfork bifurcation point. As the two outer branches correspond to the two conjugate solutions it follows that

$$\omega(x, y, t, \sigma) = -\omega(x, -y, t + 1/2, -\sigma). \tag{5.4}$$

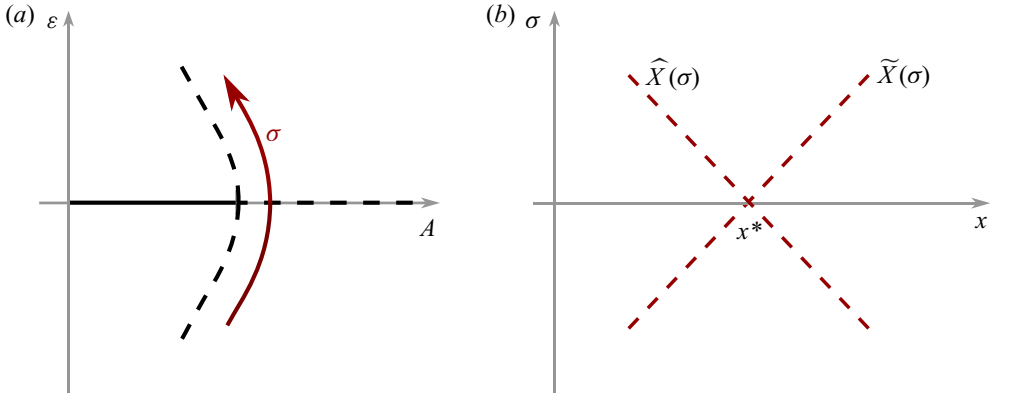

Figure 8. (*a*) A bifurcation diagram illustrating the subcritical pitchfork bifurcation. The branches of stable and unstable solutions are represented by thick lines and dashed lines, respectively. (*b*) The bifurcation diagram in a neighbourhood of $(x, \sigma) = (x^*, 0)$. Two different cusp bifurcation curves are parameterised by $\hat{X}$ and $\tilde{X}$.

We start by considering a non-degenerate critical point in the vorticity field for $\sigma = 0$, i.e. a point (x^*, y^*, t^*) satisfying

$$\left.\begin{aligned} \partial_x\omega(x^*, y^*, t^*, 0) &= 0, \\ \partial_y\omega(x^*, y^*, t^*, 0) &= 0, \\ |\boldsymbol{H}^\omega(x^*, y^*, t^*, 0)| &\neq 0. \end{aligned}\right\} \tag{5.5}$$

The implicit function theorem ensures that the critical point is preserved for sufficiently small values of $|\sigma|$. Furthermore, the continuity of $\boldsymbol{H}^\omega$ guarantees that $|\boldsymbol{H}^\omega|$ will not change sign, which means that a critical point identified as a vortex will persist. In the case where all critical points in the symmetric vorticity field are non-degenerate, the vortices persist when the symmetry is broken and no topological bifurcations occur as a direct result of the dynamical bifurcation.

If, on the other hand, the symmetric vorticity field at $\sigma = 0$ has topological variations downstream, then there exists a cusp bifurcation point (x^*, y^*, t^*) satisfying

$$\left.\begin{aligned} \partial_x\omega(x^*, y^*, t^*, 0) &= 0, \\ \partial_y\omega(x^*, y^*, t^*, 0) &= 0, \\ |\boldsymbol{H}^\omega(x^*, y^*, t^*, 0)| &= 0, \\ \mathrm{tr}(\boldsymbol{H}^\omega(x^*, y^*, t^*, 0)) &\neq 0. \end{aligned}\right\} \tag{5.6}$$

To characterise the topological changes that occur at $\sigma = 0$ we need to assume some regularity at the cusp bifurcation point (x^*, y^*, t^*). Consider the following Jacobian

$$\boldsymbol{J}_* = \left.\begin{pmatrix} \partial_{xx}\omega & \partial_{xy}\omega & \partial_{xt}\omega \\ \partial_{xy}\omega & \partial_{yy}\omega & \partial_{yt}\omega \\ \partial_x|\boldsymbol{H}^\omega| & \partial_y|\boldsymbol{H}^\omega| & \partial_t|\boldsymbol{H}^\omega| \end{pmatrix}\right|_{(x^*,y^*,t^*,0)}. \tag{5.7}$$

If the determinant of $\boldsymbol{J}_*$ is non-zero, i.e.

$$\left(-\left|\begin{pmatrix} \partial_{xx}\omega & \partial_{xy}\omega \\ \partial_x|\boldsymbol{H}^\omega| & \partial_y|\boldsymbol{H}^\omega| \end{pmatrix}\right| \partial_{yt}\omega + \left|\begin{pmatrix} \partial_{xy}\omega & \partial_{yy}\omega \\ \partial_x|\boldsymbol{H}^\omega| & \partial_y|\boldsymbol{H}^\omega| \end{pmatrix}\right| \partial_{xt}\omega\right)\Bigg|_{(x^*,y^*,t^*,0)} \neq 0, \tag{5.8}$$

it follows from the implicit function theorem that there exist unique local functions $x = \hat{X}(\sigma)$, $y = \hat{Y}(\sigma)$, $t = \hat{T}(\sigma)$ satisfying

$$\hat{X}(0) = x^*, \quad \hat{Y}(0) = y^*, \quad \hat{T}(0) = t^*, \tag{5.9a–c}$$

and

$$\left.\begin{aligned} \partial_x\omega(\hat{X}(\sigma), \hat{Y}(\sigma), \hat{T}(\sigma), \sigma) = 0, \\ \partial_y\omega(\hat{X}(\sigma), \hat{Y}(\sigma), \hat{T}(\sigma), \sigma) = 0, \\ |\boldsymbol{H}^\omega(\hat{X}(\sigma), \hat{Y}(\sigma), \hat{T}(\sigma), \sigma)| = 0. \end{aligned}\right\} \tag{5.10}$$

The functions $\hat{X}$, $\hat{Y}$ and $\hat{T}$ provide a parametric representation of a curve of topological cusp bifurcations. The shape of the bifurcation curve is given by the derivatives of $\hat{X}$, $\hat{Y}$ and $\hat{T}$ at the bifurcation point $\sigma = 0$. By implicit differentiating the equations in (5.10) we obtain the following system of equations,

$$\boldsymbol{J}_* \begin{pmatrix} \hat{X}'(0) \\ \hat{Y}'(0) \\ \hat{T}'(0) \end{pmatrix} = \begin{pmatrix} \partial_{x\sigma}\omega(x^*, y^*, t^*, 0) \\ \partial_{y\sigma}\omega(x^*, y^*, t^*, 0) \\ \partial_\sigma|\boldsymbol{H}^\omega(x^*, y^*, t^*, 0)| \end{pmatrix}. \tag{5.11}$$

As $\boldsymbol{J}_*$ is non-singular the explicit expressions of $\hat{X}'(0)$, $\hat{Y}'(0)$ and $\hat{T}'(0)$ are well-defined as a combination of the elements in the Jacobian and the right-hand side of (5.11). Rather than computing the explicit expressions, we consider a second bifurcation point that is a necessary result of the symmetry for $\sigma = 0$. From the condition in (5.4) it follows that

$$\left.\begin{aligned} \partial_x\omega(x^*, -y^*, t^* + 1/2, 0) = -\partial_x\omega(x^*, y^*, t^*, 0) = 0, \\ \partial_y\omega(x^*, -y^*, t^* + 1/2, 0) = \partial_y\omega(x^*, y^*, t^*, 0) = 0, \\ |\boldsymbol{H}^\omega(x^*, -y^*, t^* + 1/2, 0)| = |\boldsymbol{H}^\omega(x^*, y^*, t^*, 0)| = 0, \\ \operatorname{tr}(\boldsymbol{H}^\omega(x^*, -y^*, t^* + 1/2, 0)) = -\operatorname{tr}(\boldsymbol{H}^\omega(x^*, y^*, t^*, 0)) \neq 0, \end{aligned}\right\} \tag{5.12}$$

and

$$\begin{aligned} &\left(-\begin{vmatrix} \partial_{xx}\omega & \partial_{xy}\omega \\ \partial_x|\boldsymbol{H}^\omega| & \partial_y|\boldsymbol{H}^\omega| \end{vmatrix}\partial_{yt}\omega + \begin{vmatrix} \partial_{xy}\omega & \partial_{yy}\omega \\ \partial_x|\boldsymbol{H}^\omega| & \partial_y|\boldsymbol{H}^\omega| \end{vmatrix}\partial_{xt}\omega\right)\Bigg|_{(x^*,-y^*,t^*+1/2,0)} \\ &= \left(-\begin{vmatrix} -\partial_{xx}\omega & \partial_{xy}\omega \\ \partial_x|\boldsymbol{H}^\omega| & -\partial_y|\boldsymbol{H}^\omega| \end{vmatrix}\partial_{yt}\omega + \begin{vmatrix} \partial_{xy}\omega & -\partial_{yy}\omega \\ \partial_x|\boldsymbol{H}^\omega| & -\partial_y|\boldsymbol{H}^\omega| \end{vmatrix}(-\partial_{xt}\omega)\right)\Bigg|_{(x^*,y^*,t^*,0)} \\ &= \left(-\begin{vmatrix} \partial_{xx}\omega & \partial_{xy}\omega \\ \partial_x|\boldsymbol{H}^\omega| & \partial_y|\boldsymbol{H}^\omega| \end{vmatrix}\partial_{yt}\omega + \begin{vmatrix} \partial_{xy}\omega & \partial_{yy}\omega \\ \partial_x|\boldsymbol{H}^\omega| & \partial_y|\boldsymbol{H}^\omega| \end{vmatrix}\partial_{xt}\omega\right)\Bigg|_{(x^*,y^*,t^*,0)} \neq 0. \end{aligned} \tag{5.13}$$

As expected, we can therefore conclude that $(x^*, -y^*, t^* + 1/2)$ is a cusp bifurcation point satisfying all the same conditions as (x^*, y^*, t^*). By a similar argument, there exist functions $x = \tilde{X}(\sigma)$, $y = \tilde{Y}(\sigma)$ and $t = \tilde{T}(\sigma)$ that provide a parametric representation of a topological cusp bifurcation curve through the point $(x, y, t, \sigma) = (x^*, -y^*, t^* + 1/2, 0)$.

By implicit differentiation we obtain the following system of equations

$$\begin{pmatrix} \partial_{xx}\omega & \partial_{xy}\omega & \partial_{xt}\omega \\ \partial_{xy}\omega & \partial_{yy}\omega & \partial_{yt}\omega \\ \partial_x|\boldsymbol{H}^\omega| & \partial_y|\boldsymbol{H}^\omega| & \partial_t|\boldsymbol{H}^\omega| \end{pmatrix} \begin{pmatrix} \tilde{X}'(0) \\ \tilde{Y}'(0) \\ \tilde{T}'(0) \end{pmatrix} = \begin{pmatrix} \partial_{x\sigma}\omega \\ \partial_{y\sigma}\omega \\ \partial_\sigma|\boldsymbol{H}^\omega| \end{pmatrix}\Bigg|_{(x^*,-y^*,t^*+1/2,0)}, \tag{5.14}$$

which, by the symmetry condition in (5.4), can be rewritten as

$$\begin{pmatrix} -\partial_{xx}\omega & \partial_{xy}\omega & -\partial_{xt}\omega \\ \partial_{xy}\omega & -\partial_{yy}\omega & \partial_{yt}\omega \\ \partial_x|\boldsymbol{H}^\omega| & -\partial_y|\boldsymbol{H}^\omega| & \partial_t|\boldsymbol{H}^\omega| \end{pmatrix} \begin{pmatrix} \tilde{X}'(0) \\ \tilde{Y}'(0) \\ \tilde{T}'(0) \end{pmatrix} = \begin{pmatrix} \partial_{x\sigma}\omega \\ -\partial_{y\sigma}\omega \\ -\partial_\sigma|\boldsymbol{H}^\omega| \end{pmatrix}\Bigg|_{(x^*,y^*,t^*,0)}. \tag{5.15}$$

Upon comparison with the system of equations in (5.11), we note that the only difference is the sign of some elements of the Jacobian and the right-hand side. Hence, it is straightforward to show that the parametric representations of the two bifurcation curves are related in the following way,

$$\left.\begin{aligned} \tilde{X}'(0) &= -\hat{X}'(0), \\ \tilde{Y}'(0) &= \hat{Y}'(0), \\ \tilde{T}'(0) &= -\hat{T}'(0). \end{aligned}\right\} \tag{5.16}$$

There are no conditions on the derivatives of ω that make us expect that the explicit expressions of $\hat{X}'(0)$, $\hat{Y}'(0)$ and $\hat{T}'(0)$ are zero. Therefore, we assume that this is not the case in general. In figure 8(*b*) the two parametric representations of the x-coordinates of the bifurcation curves are illustrated in a neighbourhood of $(x, \sigma) = (x^*, 0)$. As shown in the figure, the x-coordinates of the cusp bifurcation points separate as σ is increased (or decreased) from zero. To summarise: for the symmetric vorticity field cusp bifurcations come in pairs, one at a point (x^*, y^*), the other at $(x^*, -y^*)$, exactly half a period later. Moving along one of the asymmetric branches and away from the symmetric branch, one bifurcation point moves upstream, and one moves downstream, Furthermore, the time separation between the two bifurcations is no longer exactly half a period.

6. Numerical results

6.1. $Re = 100$

With the numerical method described in § 3 we perform simulations where the cylinder oscillates with an amplitude in the range $0.8 \leq A \leq 1.2$ and with one of the four selected wavelengths $\lambda = 5.5$, 6.085, 6.5 and 6.7. In each simulation we keep track of the vorticity extrema during a complete oscillation cycle, and each time we observe a cusp bifurcation, we record the coordinate set of the bifurcation point (x^*, y^*, t^*). For each of the four selected wavelengths we perform simulations with more than 30 different amplitudes. We show the most interesting feature of the cusp bifurcation, i.e. its downstream location x^*, in (x, A) bifurcation diagrams in figure 9(*c*)–9(*j*). From Matharu *et al.* (2021) we know that a bistable region exists for $\lambda = 6.085$. To resolve both of these topologically different solutions, we construct two bifurcation diagrams for each of the four wavelengths. To construct the diagrams in the left column, we use a solution obtained for $A < A_1$ as the initial condition for the solution at a slightly larger A, as illustrated in figure 9(*a*). By repeating this process we can locate A_2 as the value of A where the solution jumps from the symmetric branch to the asymmetric branch. The diagrams in the right column are

constructed in a similar way but from simulations where the amplitude is decreased, as illustrated in figure 9(*b*). This yields the value A_1 when the solution jumps from the asymmetric branch to the symmetric branch. In all four cases, the bifurcation diagrams in the left and right columns differ in a small region, implying that a bistable region exists for all the four wavelengths. In other words, the dynamical bifurcation remains subcritical for all wavelengths considered. The red lines at A_1 and A_2 mark the lower and upper limits of the bistable regions. For $\lambda = 6.085$, we found that $A_1 \approx 1.078$ and $A_2 \approx 1.093$. These values are comparable to, but not exactly the same as, those determined by Matharu *et al.* (2021), i.e. $A_1 \approx 1.068$ and $A_2 \approx 1.086$. This discrepancy may be due to the difference in the numerical method used and the fact that we use a domain of different length: Matharu *et al.* (2021) used $L_{outlet} = 30$ rather than $L_{outlet} = 70$ in the present study. However, the very small variations between the values of A_1 and A_2 obtained in the two studies is an indication that the subcritical pitchfork bifurcation has been identified correctly.

As expected, each pair of bifurcation diagrams are identical outside the bistable region. That is, the curves separating the 2P and the 2S regions below A_1 and the curves separating the 2P from the P + S region above A_2 are pairwise identical. We recall that the solutions for $A < A_1$ satisfy the symmetry condition (5.1). This implies that two cusp bifurcations occur with exactly half a period in between at the same downstream position at bifurcation points marked in the (x, A) parameter plane. For the solutions which form the basis of the diagrams in the left column, the symmetry condition is satisfied for amplitude values up to $A = A_2$.

As illustrated in figure 3 we use a non-uniformly refined mesh in the region close to the cylinder. The derivative recovery method we employ, as described in § 3, is only accurate on a uniform mesh (Zienkiewicz & Zhu 1992). Therefore, we cannot resolve the cusp bifurcations that occur for $x < 5$ where the vortices are initially created. We only show the region for $x < 40$, as no topological bifurcations are observed beyond that limit.

The four pairs of bifurcation diagrams in figure 9 are qualitatively very similar. We start by considering the case where the cylinder oscillates with the Strouhal frequency, i.e. $\lambda = 6.085$, and describe in detail the corresponding pair of bifurcation diagrams in figure 9(*e*,*f*). The bifurcation curves and the upper/lower limits of the bistable region separate the (x, A) parameter plane into three distinct regions. The labels indicate whether a specific part of the wake has a 2S, 2P or a P + S topology. Let us describe the transition we observe for increasing amplitude values, as illustrated in figure 9(*e*). For amplitude values below the dashed blue line at A_0 we observe a 2S pattern that persists in the downstream wake and, hence, we classify the wake mode as $(2S)^{\infty}$. At $A = A_0$, a degenerate critical point appears at $x \approx 16$, marked with a blue cross, which immediately disappears again. As a consequence of the symmetry condition in (5.1) a degenerate critical point also appears and disappears at the same downstream position half a period later. For amplitude values slightly larger than A_0, two cusp bifurcations occur every half period. In the first bifurcation a vortex is created, and in the other the vortex is destroyed. Because these vortices persist for less than a period, we classify the wake pattern as $(2S)^2(2P)^1(2S)^{\infty}$. As we increase the amplitude further, the first cusp bifurcation point moves upstream and eventually out of the domain we consider. This implies that the two extra vortices in the 2P group are created further upstream and, hence, they persist longer. When they persist for more than an entire period, the local pattern changes from $(2P)^1$ to $(2P)^2$, and when the amplitude increases further, it changes to a $(2P)^3$ pattern. For $A = 1.05$, the extra vortices in the 2P group are created upstream of the domain we consider and they move downstream for between two and three periods before they disappear again in a cusp bifurcation. We therefore classify the topological structure of

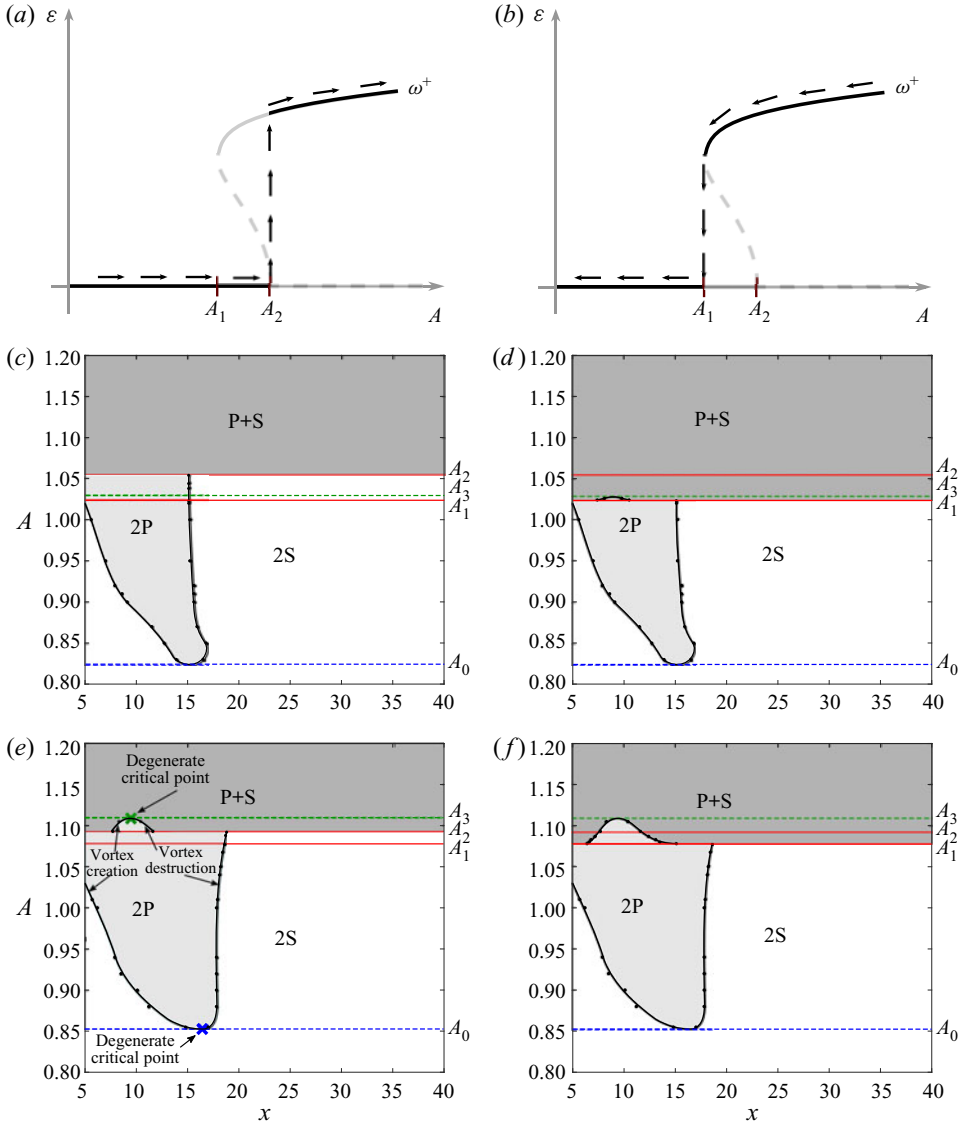

Figure 9. For caption see next page.

the wake as $(2P)^3(2S)^\infty$. At an amplitude $A = A_2$, we observe a jump from one solution branch to another accompanied by a discontinuous change in the topology to a wake that we classify as $(P + S)^1(2P)^1(P + S)^\infty$. As we increase the amplitude further and reach $A = A_3$, the two cusp bifurcation points that bound the 2P region merge and disappear at the point marked with a green cross at $x \approx 10$. For amplitude values above A_3, we observe a P + S pattern that persists in the downstream wake. Hence, we classify the wake mode as $(P + S)^\infty$.

For decreasing amplitude values, the transition from $(P + S)^\infty$ to $(2S)^\infty$ is illustrated in figure 9(*f*). The transition is essentially the reverse of the process described previously. The only difference is that the discontinuous change in the topology occurs at $A = A_1$ and, hence, the $(P + S)^n(2P)^m(P + S)^\infty$ patterns exist only above that value of A.

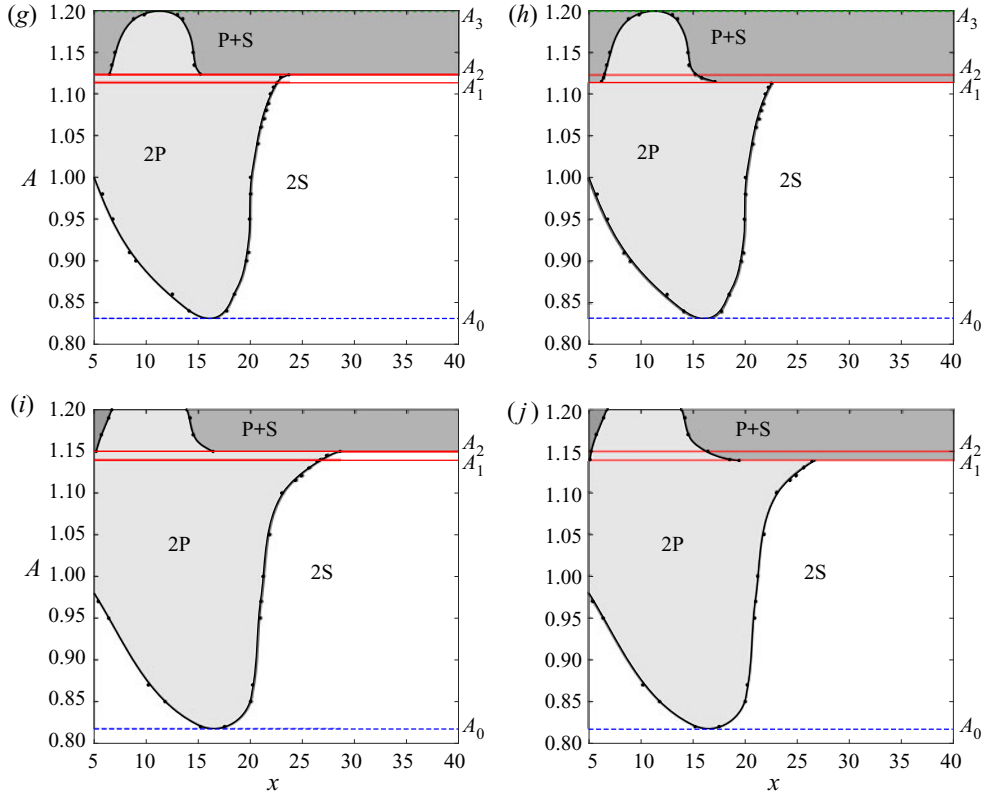

Figure 9 (cntd). (*a*), (*b*) A sketch of the dynamical bifurcation diagram illustrating one of the solution branches in the subcritical pitchfork bifurcation: (*a*) increasing A; (*b*) decreasing A. The solid black lines highlight the section of the solution curve that we explore with the simulations obtained by either increasing or decreasing the amplitude from a previous simulation. (*c*)–(*j*) Four pairs of bifurcation diagrams constructed from simulations with different wavelengths. The significance of the various elements are shown in (*e*): (*c*) $\lambda = 5.5$, increasing A; (*d*) $\lambda = 5.5$, decreasing A; (*e*) $\lambda = 6.085$, increasing A; (*f*) $\lambda = 6.085$, decreasing A; (*g*) $\lambda = 6.5$, increasing A; (*h*) $\lambda = 6.5$, decreasing A; (*i*) $\lambda = 6.7$, increasing A; and (*j*) $\lambda = 6.7$, decreasing A. The black dots, connected by solid lines, mark the downstream location of the topological bifurcation points x^* observed in the simulations. The upstream bifurcations are vortex creation, the downstream bifurcations are vortex destruction. The curves meet at degenerate critical points marked by a blue and a green cross. The dashed blue line at A_0 indicates the limit below which we observe a $(2S)^\infty$ pattern. The dashed green line at A_3 indicates the limit above which we observe a $(P+S)^\infty$ pattern. The red lines at A_1 and A_2 indicate the boundaries of the bistable region.

The remaining three pairs of bifurcation diagrams in figure 9 are constructed from simulations where the wavelength is either decreased or increased from $\lambda = 6.085$. In all four cases we observe similar wake patterns with the same topological transitions. In general, there is an A_0 such that the wake pattern is $(2S)^\infty$ for $A < A_0$ and an A_3 such that the wake pattern is $(P+S)^\infty$ for $A > A_3$. For $\lambda = 6.7$, A_3 is beyond the amplitude range we consider but from a few additional simulations, we have established that A_3 in this case is somewhere between $A = 1.27$ and $A = 1.30$.

The quantities we depict in figure 9(*c–j*), i.e. A_0, A_1, A_2, A_3 and the topological bifurcation points x^* which define the boundaries between different wake regions for each A, all depend continuously on λ. The bifurcation diagrams in figure 9 for $\lambda = 6.085, 6.5, 6.7$ are qualitatively identical. In particular, $A_3 > A_2$ in all cases. However, as λ decreases, A_3 decreases as well, and at $\lambda = 5.5$ we find that A_3 is between A_1 and A_2. This means that wakes with patterns $(P+S)^n(2P)^m(P+S)^\infty$ are not observed in figure 9(*c*).

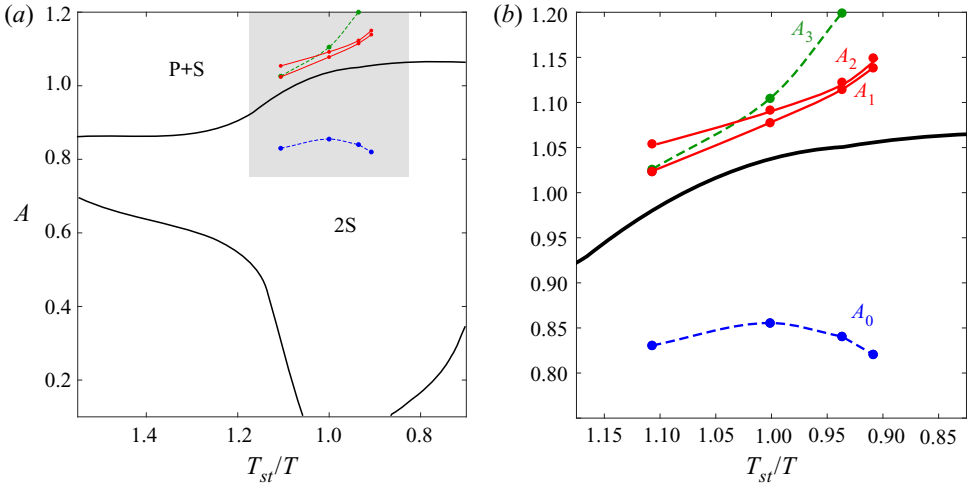

Figure 10. (*a*) A region of the parameter space explored by Leontini *et al.* (2006). The solid black lines are the boundaries of the primary synchronisation region and the boundary defining the transition from 2S to P + S, as identified by Leontini *et al.* (2006). The four characteristic amplitude values, A_0, A_1, A_2 and A_3 are marked with colors corresponding to the colors in figure 9. (*b*) A close-up of the grey region in (*a*).

These patterns only exist for $A < A_3$ on the asymmetric branch; when A is increased the jump to the asymmetric branch occurs at A_2 which for $\lambda = 5.5$ is beyond A_3. As A is decreased, however, one does reach A_3 on the asymmetric branch before jumping down to the symmetric branch at A_1. Hence, figure 9(*b*) is qualitatively identical to the other bifurcation diagrams for decreasing A.

In previous studies, where the overall pattern is determined from visual inspection, the transition between different wake modes are typically marked with a single critical boundary, indicating that there is a sharp change from one mode to another (Williamson & Roshko 1988; Leontini *et al.* 2006). Matharu *et al.* (2021) argued that for $Re = 100$ and $\lambda = \lambda_{St}$, this cannot be the correct interpretation because the symmetry-breaking pitchfork bifurcation is subcritical. It is, however, natural that the transition has been interpreted in this way previously, because a discontinuous jump in the vorticity topology is observed through simulations based on time-integration. In figure 10(*a*), we show a region of the parameter space explored by Leontini *et al.* (2006). The sharp boundary that the authors used to demarcate the transition between the 2S and P + S wake mode is drawn with a solid black line. In our search for a complete topological description of the transition, we have found that four characteristic amplitude values play an important role: the limit A_0 below which we observe $(2S)^{\infty}$, the lower and upper limits A_1, A_2 of the bistable region and the limit A_3 above which we observe $(P + S)^{\infty}$. As the results of Leontini *et al.* (2006) also derive from simulations at Re = 100, they should be directly comparable to ours. In figure 10(*a*) we have marked the four characteristic amplitude values for each of our wavelength values (or, equivalently, the corresponding periods). The coloured dots, connected by solid or dashed lines, defines a region of the parameter space in which the transition occur. It is only above and below all these lines that we can classify the pattern as a full P + S or 2S pattern.

As the symmetry-breaking pitchfork bifurcation at A_2 is subcritical, we do not observe a simple stepwise evolution of the vorticity field in the transition from 2S to P + S where the indices of the elements 2P, 2S and P + S are increased or decreased by one. This is because part of that evolution takes place along the unstable part of ω^+ (or equivalently ω^-).

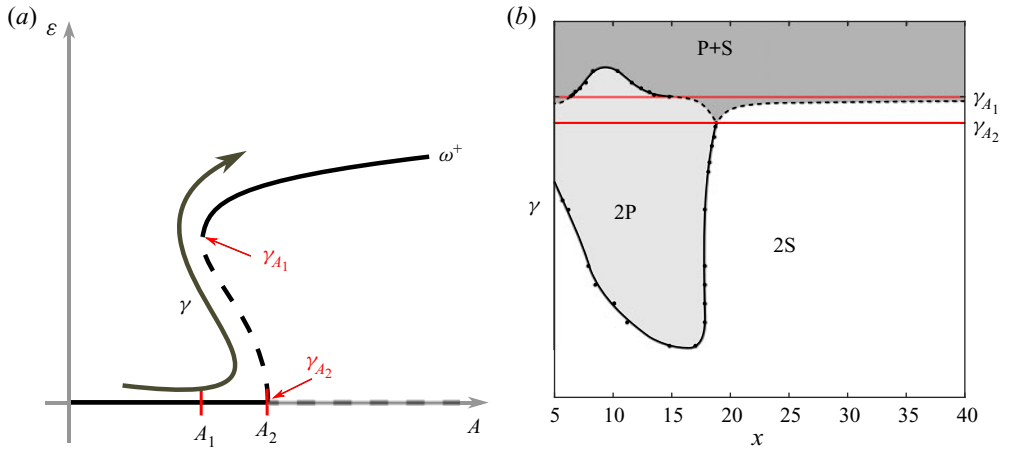

Figure 11. (*a*) A sketch of the dynamical bifurcation diagram near $A = A_2$ reparameterised by the parameter γ. (*b*) A bifurcation diagram in the (x, γ) parameter plane. The black dots, connected by solid lines, mark the bifurcation points observed in the simulations with $\lambda = 6.085$. The dashed lines in the range $\gamma_{A_2} < \gamma < \gamma_{A_1}$ are examples of how the bifurcation curves could evolve along the unstable solution branch.

However, based on the theoretical considerations in § 5, we can still give a complete qualitative picture of the topological changes in the transition from 2S to P + S. We introduce a path parameterised by a parameter γ that switches from the stable symmetric branch onto the unstable asymmetric branch when reaching the pitchfork bifurcation point at $A = A_2$, see figure 11(*a*). In figure 11(*b*) we illustrate the (x, γ) parameter plane for $\lambda = 6.085$. The solutions for $\gamma < \gamma_{A_2}$ and $\gamma > \gamma_{A_1}$ lie on the stable branches and are topologically described by the preceding analysis of the numerical simulations. The bifurcation curves drawn as solid lines in figure 11(*b*) are therefore identical to those shown in figures 9(*e*) and 9(*f*). The time-periodic solutions in the region $\gamma_{A_2} < \gamma < \gamma_{A_1}$ lie on the unstable branch. Based on the result in § 5, we know that as soon as the symmetry is broken at $\gamma = \gamma_{A_2}$, one of the cusp bifurcation points moves upstream and the other moves downstream. These bifurcations occur at the two dashed black curves in figure 11(*b*) that split at $\gamma = \gamma_{A_2}$. The left bifurcation curve separates a 2P region upstream from a P + S region downstream. The right bifurcation curve separates a P + S region upstream from a 2S region downstream. When γ is increased beyond γ_{A_1}, and the periodic solution becomes stable, the simulations show a cusp bifurcation curve that separates a 2P region from a P + S region; this bifurcation curve must be connected to the left dashed bifurcation curve emanating from γ_{A_2}. In the stable regime $\gamma > \gamma_{A_1}$ no bifurcations separating P + S from 2S are observed. Therefore, the right dashed curve must leave the domain we consider for $\gamma < \gamma_{A_1}$, as indicated in figure 11(*b*). Hence, when γ is increased from γ_{A_2} to γ_{A_1} there must be a succession of patterns $(2P)^3(P + S)^n(2S)^\infty$ where n grows rapidly with γ, pushing the $(2S)^\infty$ part out into the very far wake which we do not consider here.

With this extended bifurcation diagram we have a complete qualitative picture of the topological changes in the transition from 2S to P + S, despite a significant part of the transition being invisible due to the topological changes taking place along the unstable branch.

6.2. $Re = 80$

The analysis at $Re = 100$ in the previous subsection shows that the transition of the wake from a 2S to a P + S pattern goes through a series of topological bifurcations both at

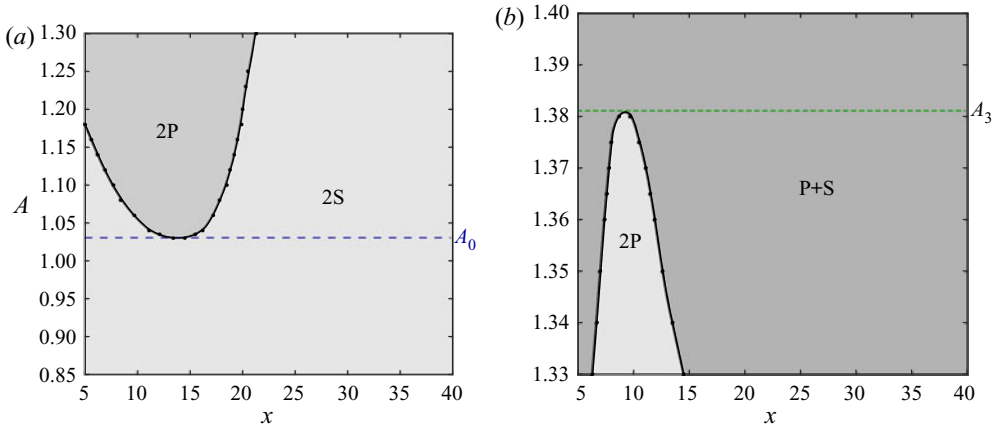

Figure 12. Topological bifurcation diagrams for $Re = 80$ at the Strouhal wavelength $\lambda = 6.5437$. (*a*) The symmetric branch below the bistable range. (*b*) The asymmetric branch for A just above the first dynamical cusp bifurcation point A_{F1}. As in figures 9(*c*)–9(*j*), the black curves mark topological cusp bifurcations.

the symmetric and the asymmetric branch. To investigate the robustness of this scenario, we briefly consider $Re = 80$ at the Strouhal wavelength $\lambda = 6.544$. Matharu *et al.* (2021) show that there is no dynamical pitchfork bifurcation here; the symmetric state is stable for all values of A. However, two branches of asymmetric solutions, one branch stable, one branch unstable, with no connection to the symmetric branch, exist for A between A_{F1} and A_{F2} with $A_{F1} \approx 1.3145$ and $A_{F2} \approx 1.4988$. At A_{F1} and A_{F2} the two branches merge in dynamical fold bifurcations, forming a so-called isola. Hence, for $A_{F1} < A < A_{F2}$ the system is bistable. Here we explore the topological bifurcations of the wake as A is varied up to and above A_{F1}.

Figure 12 shows topological bifurcation diagrams similar to those in figure 9. Figure 12(*a*) shows bifurcations at the symmetric branch below A_{F1}. As for $Re = 100$, we see there is an $A_0 \approx 1.003$ below which the wake pattern is $2S^{\infty}$. Above A_0, local patterns $(2P)^n$ appear and disappear through topological cusp bifurcations. The first cusp bifurcation moves upstream as A is increased, finally yielding patterns of the form $(2P)^n(2S)^{\infty}$. Figure 12(*b*) shows the asymmetric branch just above A_{F1}. As for $Re = 100$ at the asymmetric branch above A_1, there are local patterns both of type $(2P)^n$ and $(P + S)^m$. As A is increased, the $(2P)^n$ region shrinks and, finally, disappears at $A_3 \approx 1.381$.

Even if the symmetric branch is stable for all values of A, the rate of attraction is very small in the bistable range $A > A_{F1}$, requiring prohibitively long computations to resolve the flow completely. Except for A very close to A_{F1}, the convergence to the asymmetric branch is much faster, and it appears from simulations that the asymmetric branch attracts solutions with initial conditions even very close to the symmetric branch. This implies that, for any practical purpose, in the bistable range only the asymmetric branch will be actually be attained after transients. To reach the symmetric branch here, the initial condition must be very close to the limit cycle, and even very small perturbations will drive the solution away to the asymmetric branch. Hence, in practice, the symmetric branch is unstable for $A > A_{F1}$, and A_{F1} will act as a bifurcation point where the solution jumps from the symmetric branch to the asymmetric branch as A is increased. Decreasing A for a solution on the asymmetric branch, the solution will jump to the symmetric branch at A_{F1}.

In summary, as for $Re = 100$ we find two key topological bifurcation points: A_0, below which the wake pattern is $(2S)^{\infty}$ and A_3, above which the pattern is $(P + S)^{\infty}$. For A

between these values there are mixed patterns. In addition, there is a dynamical bifurcation point A_{F1} between A_0 and A_3 where the periodic solution switches between the symmetric and the asymmetric branch. For $Re = 100$ there are two such points, A_1 and A_2, which leads to hysteresis not present at $Re = 80$, but otherwise the transition scenarios at $Re = 100$ and $Re = 80$ are qualitatively identical.

7. Summary

We have investigated the topological changes of the vorticity field in the transition from 2S to P + S wake mode at $Re = 100$. The transition cannot be fully described with a single critical boundary. Instead of a sharp change from one mode to another, we determine a range of amplitude values where the corresponding wake has a mixed pattern with topological variations downstream. We show that the symmetry-breaking pitchfork bifurcation identified by Matharu *et al.* (2021) plays an important role in the transition, but at the same time it does not provide the complete description, as topological changes occur even before this bifurcation point. In general, the transition can be described as follows: through a continuous evolution of the vorticity field, a 2P-like pattern arises in near wake. The extra two vortices that we detect in the shear layers arise through cusp bifurcations and move downstream for up to three periods before disappearing again in two reverse cusp bifurcations separated by a half period. We prove that the topological role of the pitchfork bifurcation is to relax the condition that these two cusp bifurcations must occur with a temporal spacing of exactly half a period. The breaking of symmetry allows one of the cusp bifurcations to move rapidly downstream, implying that only one of the extra vortices persists in the downstream wake. As the second cusp bifurcation moves upstream the 2P-like pattern in the near wake disappears and the wake has a clear P + S structure. As the symmetry-breaking pitchfork bifurcation is subcritical, a significant part of the continuous evolution of the vorticity field takes place along the unstable solution branch. This part of the evolution is not visible in our simulations, but based on the theoretical considerations in § 5 we are still able to give a complete qualitative picture of the continuous transition from 2S to P + S.

In all four cases we have examined, the bistable region is so narrow that the criticality of the pitchfork bifurcation may change from subcritical to supercritical when the wavelength increases further, the Reynolds number changes or the shape of the cylinder changes. If it turns out that there are situations where the transition is supercritical, then the qualitative description will be the same and the entire continuous evolution will be visible in the simulations.

The robustness of the described scenario is confirmed by simulations performed at $Re = 80$. Although the dynamical bifurcation structure is different here, we find again a sequence of topological bifurcations in the wake leading from 2S to P + S over an interval of amplitude values. In addition, both the symmetric and asymmetric solutions exhibit wakes with topological variations.

Acknowledgements. We wish to acknowledge Professor M. Heil from University of Manchester who has supported the numerical part of the study and participated in many fruitful discussions.

Funding. Financial support from Independent Research Fund Denmark, grant no. 6108-00246B, is gratefully acknowledged.

Declaration of interests. The authors report no conflict of interest.

Author ORCIDs.
Anne R. Nielsen https://orcid.org/0000-0001-7144-8978;

Puneet S. Matharu https://orcid.org/0000-0001-9359-9814;
Morten Brøns https://orcid.org/0000-0001-5522-3410.

References

Aref, H., Stremler, M.A. & Ponta, F.L. 2006 Exotic vortex wakes-point vortex solutions. *J. Fluids Struct.* **22** (6–7), 929–940.

Barkley, D. & Henderson, R.D. 1996 Three-dimensional Floquet stability analysis of the wake of a circular cylinder. *J. Fluid Mech.* **322**, 215–241.

Bishop, R.E.D., Hassan, A.Y. & Saunders, O.A. 1964 The lift and drag forces on a circular cylinder oscillating in a flowing fluid. *Proc. R. Soc. Lond. Ser.* A. *Math. Phys. Sci.* **277** (1368), 51–75.

Blackburn, H.M. & Henderson, R.D. 1999 A study of two-dimensional flow past an oscillating cylinder. *J. Fluid Mech.* **385**, 255–286.

Blackburn, H.M., Marques, F. & Lopez, J.M. 2005 Symmetry breaking of two-dimensional time-periodic wakes. *J. Fluid Mech.* **522**, 395–411.

Brika, D. & Laneville, A. 1993 Vortex-induced vibrations of a long flexible circular cylinder. *J. Fluid Mech.* **250**, 481–508.

Brøns, M. 2007 Streamline topology: patterns in fluid flows and their bifurcations. *Adv. Appl. Mech.* **41**, 1–42.

Brøns, M. & Bisgaard, A.V. 2010 Topology of vortex creation in the cylinder wake. *Theor. Comput. Fluid Dyn.* **24** (1–4), 299–303.

Brøns, M., Jakobsen, B., Niss, K., Bisgaard, A. & Voigt, L.K. 2007 Streamline topology in the near wake of a circular cylinder at moderate Reynolds numbers. *J. Fluid Mech.* **584**, 23–43.

Carberry, J., Sheridan, J. & Rockwell, D. 2001 Forces and wake modes of an oscillating cylinder. *J. Fluids Struct.* **15** (3–4), 523–532.

Dusek, J., Le Gal, P. & Fraunie, P. 1994 A numerical and theoretical study of the first Hopf bifurcation in a cylinder wake. *J. Fluid Mech.* **264**, 59–80.

Dynnikova, G.Y., Dynnikov, Y.A., Guvernyuk, S.V. & Malakhova, T.V. 2021 Stability of a reverse Kármán vortex street. *Phys. Fluids* **33** (2), 024102.

Gioria, R.S., Jabardo, P.J.S., Carmo, B.S. & Meneghini, J.R. 2009 Floquet stability analysis of the flow around an oscillating cylinder. *J. Fluids Struct.* **25** (4), 676–686.

Godoy-Diana, R., Aider, J.-L. & Wesfreid, J.E. 2008 Transitions in the wake of a flapping foil. *Phys. Rev.* E **77** (1), 016308.

Griffin, O.M. 1971 The unsteady wake of an oscillating cylinder at low Reynolds number. *Trans. ASME* E*: J. Appl. Mech.* **38** (4), 729–738.

Heil, M. & Hazel, A.L. 2006 oomph-lib - an object-oriented multi-physics finite-element library. In *Fluid–Structure Interaction* (ed. M. Schäfer & H.-J. Bungartz), pp. 19–49. Springer.

Heil, M., Rosso, J., Hazel, A.L. & Brøns, M. 2017 Topological fluid mechanics of the formation of the Kármán-vortex street. *J. Fluid Mech.* **812**, 199–221.

Huerre, P. & Monkewitz, P.A. 1990 Local and global instabilities in spatially developing flows. *Annu. Rev. Fluid Mech.* **22** (1), 473–537.

Karasudani, T. & Funakoshi, M. 1994 Evolution of a vortex street in the far wake of a cylinder. *Fluid Dyn. Res.* **14** (6), 331–352.

Leontini, J.S., Stewart, B.E., Thompson, M.C. & Hourigan, K. 2006 Wake state and energy transitions of an oscillating cylinder at low Reynolds number. *Phys. Fluids* **18** (6), 067101.

Matharu, P.S., Hazel, A.L. & Heil, M. 2021 Spatio-temporal symmetry breaking in the flow past an oscillating cylinder. *J. Fluid Mech.* **918**, A42.

Morse, T.L. & Williamson, C.H.K. 2009 Fluid forcing, wake modes, and transitions for a cylinder undergoing controlled oscillations. *J. Fluids Struct.* **25** (4), 697–712.

Noack, B.R. & Eckelmann, H. 1994 A global stability analysis of the steady and periodic cylinder wake. *J. Fluid Mech.* **270**, 297–330.

Ponta, F.L. & Aref, H. 2006 Numerical experiments on vortex shedding from an oscillating cylinder. *J. Fluids Struct.* **22** (3), 327–344.

Sandulescu, M., Hernández-Garcìa, E., López, C. & Feudel, U. 2006 Kinematic studies of transport across an island wake, with application to the Canary Islands. *Tellus* A*: Dyn. Meteorol. Oceanogr.* **58** (5), 605–615.

Schnipper, T., Andersen, A.P. & Bohr, T. 2009 Vortex wakes of a flapping foil. *J. Fluid Mech.* **633**, 411–423.

SHARIFF, K., PULLIAM, T.H. & OTTINO, J.M. 1991 A dynamical systems analysis of kinematics in the time-periodic wake of a circular cylinder. In *Vortex Dynamics and Vortex Methoods* (ed. C.R. Anderson & C. Greengard), Lectures in Applied Mathematics, vol. 28, pp. 613–646. American Mathematical Society.

WILLIAMSON, C.H.K. 1988 Defining a universal and continuous Strouhal-Reynolds number relationship for the laminar vortex shedding of a circular-cylinder. *Phys. Fluids* **31** (10), 2742–2744.

WILLIAMSON, C.H.K. & ROSHKO, A. 1988 Vortex formation in the wake of an oscillating cylinder. *J. Fluids Struct.* **2**, 355–381.

ZIENKIEWICZ, O.C. & ZHU, J.Z. 1992 The superconvergent patch recovery and a posteriori error estimates. Part 1: the recovery technique. *Intl J. Numer. Meth. Engng* **33** (7), 1331–1364.